

# TPSC results analysis for electron doped NCCO

Pierre-Antoine Graham\*  
(Dated: November 29, 2022)

The temperature/doping phase diagram of electron-doped cuprate NCCO displays many interesting features that are partially captured by TPSC calculations for the Hubbard model. In particular, it explains the antiferromagnetic pseudogap of NCCO over most of the doping range. To quantify the predictions in a more realistic setting, I study the evolution of the Fermi liquid scattering rate and spectral weight across the Fermi surface with and without disorder (clean limit). I find that the scattering rate becomes linear in temperature at the nodal point of the Fermi surface at the quantum critical doping. Disorder does not modify the criterion for the appearance of the pseudogap, namely that the antiferromagnetic correlation length must become larger than the thermal de Broglie wavelength. In particular, the experimental observation of a pseudogap near the optimal superconducting transition temperature where the antiferromagnetic correlation length is small cannot be explained by disorder.

## CONTENTS

List of Figures	1	3 Spectral weight $A(\mathbf{k}, \omega = 0)$ for a given temperature, interaction $U$ and doping over a quarter brillouin zone. ....	5
List of Tables	2	4 Copper atom lattice with alternating spins representing the AFM phase .....	5
I. Introduction	2	5 AFM lattice taking the periodicity of the spin pattern into account .....	5
II. Fermi surface reconstruction	3	6 Normal state Brillouin zone (red square), AFM Brillouin zone (blue diamond), Fermi surface outside the AFM phase (black) and additional part of the Fermi surface associated to the AFM phase (dashed blue) .....	5
III. Quantum criticality	3	7 Schematic phase diagram containing the main features produced by the Hubbard model applied to the copper atom lattice of NCCO .....	6
IV. Hubbard Model	4	8 Schematic representation of possible hops on the copper/oxygen lattice with their associated amplitudes. The cuprate studied here is associated to $t = 1$ , $t' = -0.175$ , $t'' = 0.05$ and all other hops impossible. ....	6
V. TPSC	5	9 Schematic representation of the linear extrapolation from the first two Matsubara frequencies to the zero frequency evaluation of self-energy .....	8
VI. Results	7	10 Exponent $\nu$ giving the power law for the temperature dependance of the imaginary part of self-energy at zero frequency as a function of angle on the Fermi surface for different dopings (without disorder at $U = 5.75$ ) .....	9
A. Power law for the electron-electron scattering rate (without disorder)	7	11 Self-energy curves for matsubara frequencies for a fixed temperature and varying interaction $U$ .....	9
B. Fits on real frequency self-energy	8	12 Self-energy curves for real frequencies for a fixed temperature and varying interaction $U$	10
C. Kadowaki-Woods ratio	9	13 Fit parameters as functions of $T^2$ for different interaction $U$ values associated to colours .....	11
D. Locating the Quantum critical point with disorder	10	14 Schematic representation of the projection of the $U^2$ axis to the $T^2$ -parameter plane ..	11
E. Criteria for the pseudogap opening with disorder	14		
F. Power law for the electron-electron scattering rate (with disorder)	15		
G. Conclusion	17		
References	17		

## LIST OF FIGURES

1	Crystalline structure of NCCO [1] .....	3
2	Experimental temperature-doping phase diagram of NCCO [2] .....	4

---

\* Physics Department, Sherbrooke University.

15	Fit parameters as functions of $U^2$ for different temperatures values associated to colours .....	12
16	Schematic representation of the projection of the $T^2$ axis to the $U^2$ -parameter plane ..	12
17	Quasiparticle weight $Z$ as a function of the interaction $U$ for different temperatures giving the colour .....	13
18	$a_2$ fit parameter as a function of $U^2$ for different temperatures .....	13
19	Kadowaki-woods plot .....	13
20	Spectroscopic Kadowaki-woods plot [3] ....	13
21	Linear extrapolation estimating the doping of the quantum critical point using the doping at which the pseudogap opens for different temperatures (without disorder) .	14
22	Linear extrapolation estimating the doping of the quantum critical point using the doping at which the pseudogap opens for different temperatures (with disorder) .....	15
23	Schematic representation of the definition of hot-spots in a quarter Brillouin zone ....	15
24	Schematic representation of the different types of Spectral weight curves at the hot spots .....	15
25	Spectral weight evaluated at hot spots as a function of frequency for different temperatures (one for each plot) and different dopings (giving the color) .....	16
26	Linear extrapolation estimating the doping of the quantum critical point using the second biggest doping for which there is a local minima near $\omega = 0$ in the spectral weight evaluated at the hot-spots as a function of temperature (with disorder) ...	16
27	Order relation between the spin correlation length $\xi_{sp}$ , the thermal de Broglie length $\xi_{th}$ and the mean free path $L$ associated to disorder .....	16
28	Imaginary part of self-energy (left) and electron-electron scattering rate (right) as a function of temperatures for different angles on the Fermi surface giving the colour .	18
29	Exponent $\nu$ giving the power law for the temperature dependance of the imaginary part of self-energy at zero frequency (blue) and the electron-electron scattering rate (red) as a function of angle on the Fermi surface for the estimated quantum critical doping .....	18
30	Exponent $\nu$ giving the power law for the temperature dependance of the imaginary part of self-energy at zero frequency as a function of angle on the Fermi surface for different dopings (with disorder associated to the impurity scattering time $\tau = 46$ at $U = 5.75$ ) .....	19

## LIST OF TABLES

I	Notation for the real and imaginary parts of self-energy in Matsubara frequencies and real frequencies .....	7
II	Associations and expected dependencies on Temperature (from Fermi liquid theory) and interaction $U$ (from second order perturbation theory) for the fit parameters $a_0, a_1, a_2, b_0$ .....	10

## I. INTRODUCTION

In the past 30 years [4], research on cuprates has led to the discovery of many phenomena from the normal state to the superconducting state in these materials. As of today, they are far from being completely understood and they are studied with a large variety of theoretical and experimental techniques. During my internship, I focused on the normal state of the electron doped cuprate NCCO. The crystalline structure of this cuprate is represented on fig. 1 and its experimental temperature-doping phase diagram (electron doped part) is displayed on fig. 2. The part of the phase diagram which interests us here is the quantum critical region and its surroundings. This region emerges from a zero temperature quantum critical point which was the centre of my analysis. To get theoretical results for NCCO inside and outside of this region, I used the two particle self consistent approach (TPSC) which allows finding an approximate solution of the Hubbard model and describe the normal state. Experimentally the normal state is accessed by applying high enough magnetic fields and here the normal state is accessed theoretically by removing superconductivity-related terms from the model : leaving only the Hubbard model. The present report describes the results of my analysis for electron-electron scattering rate, Fermi-liquid behaviour and quantum criticality with and without disorder.

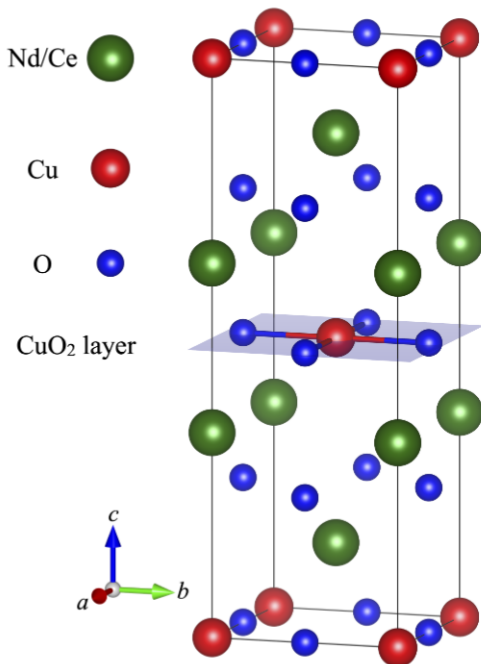


FIG. 1. Crystalline structure of NCCO [1]

## II. FERMION SURFACE RECONSTRUCTION

When NCCO enters the AFM phase, the spins of the electrons on the copper atoms organize themselves in an alternating pattern represented schematically in fig. 4 (this representation shows one electron per copper atom but in reality, at  $x \neq 0$  there is more than one electron per atom). This pattern ensures that electrons on neighbouring copper atoms have opposite spins and is favoured when the interaction is high. It repeats in a way that makes it possible to tile the copper atom plane with a new basic unit cell (see the blue vertices and associated lattice in fig 5). Electrons in this new AFM lattice will be described by a different set of Bloch waves than electrons for NCCO outside the AFM phase. Since the AFM unit cell in direct space is a diamond twice as big as the squares from the regular copper lattice, the associated Brillouin zone in reciprocal space is twice as small and is also shaped like a diamond (see fig. 6).

To go further in the description of the transition to the AFM phase the interacting equivalent of the Fermi surface has to be defined. The concept of a Fermi surface becomes less clear when interaction is turned on. Here, the interacting Fermi surface is defined to be the  $\mathbf{k}$  points in the Brillouin zone where the spectral weight (see [5] chap. 2 for a definition of the spectral weight) evaluated at  $\omega = 0$  reaches a maximum of intensity. An example of this  $\omega = 0$  spectral weight is represented in fig. 3. This Fermi surface is typical of a Fermi liquid. The Fermi surface in the normal state is typically shaped like the black

lines in fig. 6. As NCCO gets closer to the AFM phase, the Fermi surface changes to become consistent with the new periodicity. Since the AFM Brillouin zone is repeated inside the normal state Brillouin Zone, the Fermi surface has to repeat itself on each side of the AFM Brillouin zone boundary. This repetition is accomplished by adding the dashed blue part of the Fermi surface shown in fig. 6. The associated continuous transformation of the Fermi surface is called the Fermi surface reconstruction.

## III. QUANTUM CRITICALITY

The model used here to describe the behaviour of electrons in the copper planes is the Hubbard model (see sec. IV). It is a two-dimensional model which neglects the possibility of interlayer hopping thus introducing inconsistencies between theoretical results and experimental observations. In fact, interlayer hopping makes real NCCO a three-dimensional material and the two-dimensional simulated NCCO fails to recreate all its properties. A big part of the inconstancy lies the Mermin-Wagner-Hohenberg theorem (see [6] 66.2). It states that for two-dimensional systems there cannot be a continuous symmetry breaking at finite temperature. Looking back at fig 4 from sec. II, one can observe that the spins are organized in a way that breaks the continuous rotational symmetry present in the normal state. While spins have no preferred orientations in the normal state and they acquire long-range order locking spins in one direction when the AFM phase is established. As far as the two-dimensional Hubbard model goes, this kind of perfect infinite pattern for spins never occurs for non-zero temperatures as a consequence of the Mermin-Wagner-Hohenberg theorem. A two-dimensional model for NCCO lacks a clear AFM phase transition except at zero temperature where the phase changes at a single point. This point is called a quantum critical point and it is a central piece of the simplified phase diagram of fig. 7. This phase diagram is the equivalent of fig. 2 but describes two-dimensional results for NCCO and focuses on the features which will be important for the analysis done here.

Let's define the  $T^*$  line shown in fig. 7. It is obtained by plotting the temperature at which the pseudogap opens as a function of doping. The pseudogap opening is a loss of intensity in the spectral weight at  $\omega = 0$  at the hot-spots (see fig. 23 and the associated definition for hot-spots in sec. VID).  $T^*$  is a feature of the experimental phase diagram in fig. 2 where it is represented by the line included between grey and white point. The point of this line on the doping axis gives the doping for which the pseudogap opens at zero temperature. From the point of view of experimental result, this zero temperature point is separated from the beginning of the AFM phase (QCP) but in the scope of the Hubbard model it coincides with the QCP. This fact will be used

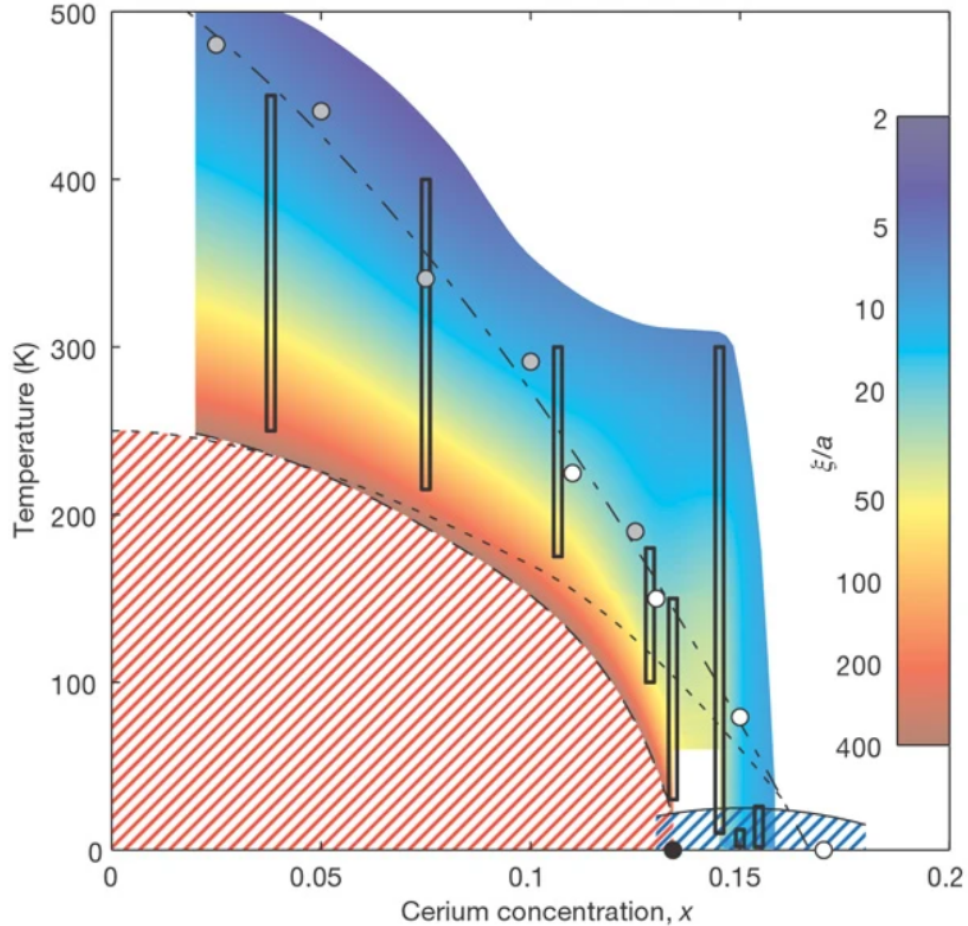


FIG. 2. Experimental temperature-doping phase diagram of NCCO [2]

in sec. VID where the location of the QCP will be estimated by linearly extrapolating from points on the  $T^*$  line determined with different approaches.

Above the QCP, the two-dimensional Hubbard model leads to a quantum critical region bounded by the  $T^*$  line and the beginning of a Fermi liquid behaviour (see sec ??) region for the temperature dependence of the electron-electron scattering rate.

#### IV. HUBBARD MODEL

With the formalism of second quantization [7] and the terminology of lattices [8] in mind, one can write a huge variety of models capturing different effects of interactions and displacements of electrons on a lattice. Here, the Hubbard's model to study the hopping of electrons in the copper/oxygen planes of NCCO. When the possibility of hopping to oxygen atoms is neglected only a square lattice of copper atoms remains (see fig. 8). Let  $c_{i\sigma}$  be an operator creating an electron on site  $i$  of the

copper lattice with a spin  $\sigma$ . Its hermitian conjugate is the corresponding annihilation operator. Since we only consider one orbital of copper atoms, the Pauli principle forbids the presence of more than one electron with the same spin on a given site. Knowing that, we can write the Hamiltonian  $H$  governing the evolution of electrons on the copper sites by adding a kinetic hopping term to a term counting how many sites are occupied by two electrons. The kinetic term is the sum of all possible displacements (annihilation followed by creation) of electrons to a neighbouring site on the lattice. Each hop has an amplitude depending on the distance with the associated neighbour. The double occupation term accounts for the interaction of electrons at the same site and is weighted by a scalar  $U$  giving the strength of the interaction. We neglect the interaction between electrons that are not on the same site. All of these details lead to the Hamiltonian:

$$H = -t \sum_{\langle ij \rangle, \sigma} c_{j\sigma}^\dagger c_{i\sigma} - t' \sum_{\langle\langle ij \rangle\rangle, \sigma} c_{j\sigma}^\dagger c_{i\sigma} - t'' \sum_{\langle\langle\langle ij \rangle\rangle\rangle, \sigma} c_{j\sigma}^\dagger c_{i\sigma} + U \sum_i n_{i\uparrow} n_{i\downarrow}$$

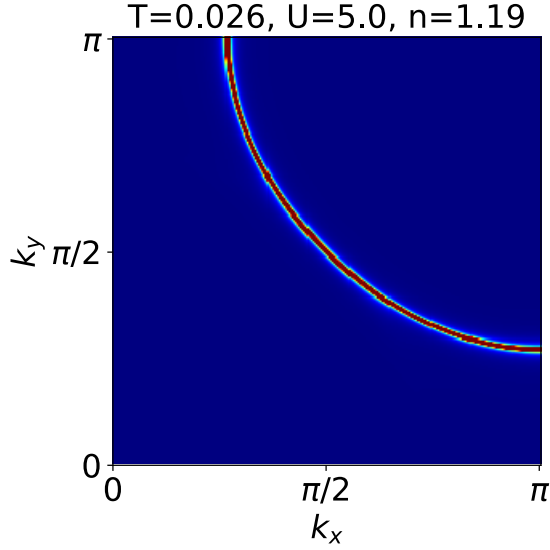


FIG. 3. Spectral weight  $A(\mathbf{k}, \omega = 0)$  for a given temperature, interaction  $U$  and doping over a quarter brillouin zone.

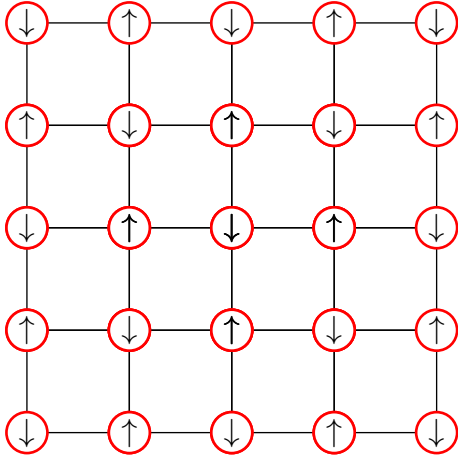


FIG. 4. Copper atom lattice with alternating spins representing the AFM phase

where  $\langle ij \rangle$  denotes the hopping combination identified with the  $t$  amplitude,  $\langle\langle ij \rangle\rangle$  denotes the hopping combination identified with the  $t'$  amplitude and  $\langle\langle\langle ij \rangle\rangle\rangle$  corresponds to the terms identified by  $t''$  in figure 8. Taking  $U = 0$ , one gets the non-interacting propagation of electrons on the planes. The model then becomes exactly solvable by rewriting the Hamiltonian with the creation and annihilation operators for planar waves with wavevector  $\mathbf{k} = (k_x, k_y)$  in the reciprocal space. The  $\mathbf{k}$  states are energy eigenstates and the energy of an electron in such a state is given by

$$\epsilon(\mathbf{k}) = -2t (\cos(k_y) + \cos(k_x)) - 4t' \cos(k_y) \cos(k_x) - 2t'' (\cos(2k_y) + \cos(2k_x)).$$

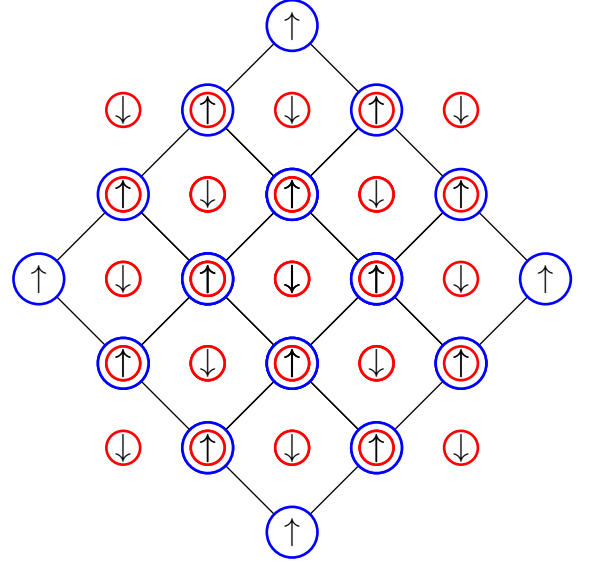


FIG. 5. AFM lattice taking the periodicity of the spin pattern into account

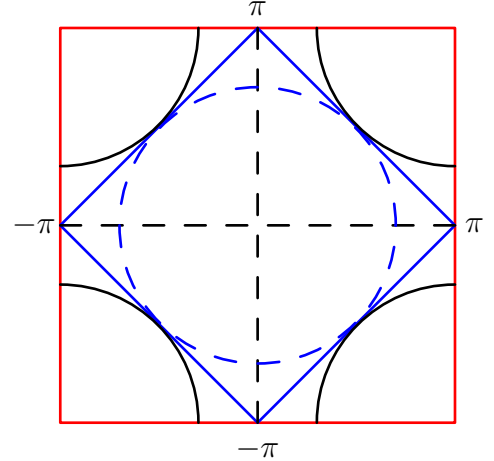


FIG. 6. Normal state Brillouin zone (red square), AFM Brillouin zone (blue diamond), Fermi surface outside the AFM phase (black) and additional part of the Fermi surface associated to the AFM phase (dashed blue)

## V. TPSC

TPSC stands for Two Particle Self-Consistent approach. It is the theoretical foundation of the main algorithm used to produce all of the results presented here. This section aims to give a simple description of the main steps of the TPSC algorithm (see [9] and [6] chap. 57, 58 for more detail).

The goal of TPSC is to approximate (in a non-perturbative way) a solution to the Hubbard model that respects the Mermin-Wagner-Hohenberg theorem and the Pauli exclusion principle. In the end this approximate solution takes the form of a second-order approx-

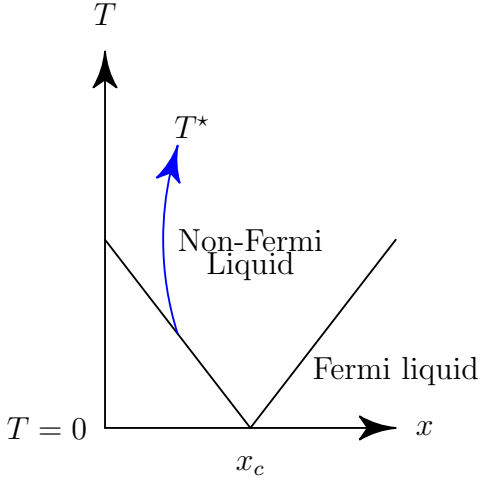


FIG. 7. Schematic phase diagram containing the main features produced by the Hubbard model applied to the copper atom lattice of NCCO

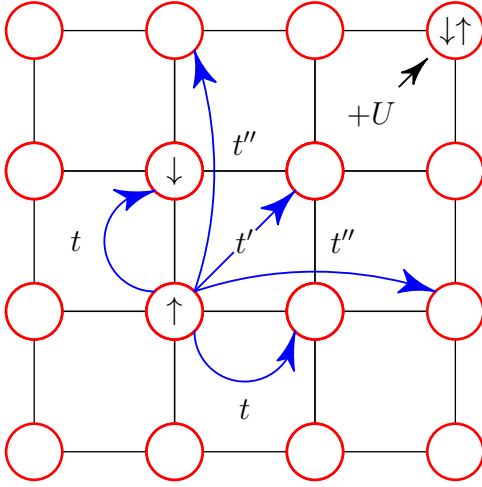


FIG. 8. Schematic representation of possible hops on the copper/oxygen lattice with their associated amplitudes. The cuprate studied here is associated to  $t = 1$ ,  $t' = -0.175$ ,  $t'' = 0.05$  and all other hops impossible.

imation of self-energy accompanied by many quantities obtained in intermediate calculations. To get to this self-energy, the Lindhard function  $\chi_0(q)$ , the spin response function  $\chi_{sp}(q)$  and the charge response function  $\chi_{ch}(q)$  are computed. The spin and charge response functions are expressed with the Lindhard function in the following way

$$\chi_{sp}(q) = \frac{\chi_0(q)}{1 - \frac{1}{2}U_{sp}\chi_0(q)},$$

$$\chi_{ch}(q) = \frac{\chi_0(q)}{1 + \frac{1}{2}U_{ch}\chi_0(q)}.$$

Note that  $q$  refers to both a reciprocal space point  $\mathbf{q}$ , a Matsubara frequency  $q_n$  associated to the temperature for the calculations and a spin index. The quantity  $\epsilon(\mathbf{q})$ .

The quantities  $U_{sp}$  and  $U_{ch}$  are the main unknowns of TPSC. To solve for them an approximate ansatz is set for  $U_{sp}$ :

$$U_{sp} = \frac{\langle n_{\uparrow}n_{\downarrow} \rangle}{\langle n_{\uparrow} \rangle \langle n_{\downarrow} \rangle}.$$

This ansatz depends on the double occupation  $\langle n_{\uparrow}n_{\downarrow} \rangle$  and on the average of up and down spins ( $\langle n_{\uparrow} \rangle$ ,  $\langle n_{\downarrow} \rangle$ ). Generally, these quantities depend on the position of direct space where they are evaluated, but because of the translational symmetry of the system they are taken invariant of position. Rotational invariance in the normal state leads to  $\langle n_{\downarrow} \rangle = \langle n_{\uparrow} \rangle = n/2$ . Therefore the only real unknown in  $U_{sp}$  is the double occupation.

The main equations of TPSC are sum rules for  $\chi_{sp}(q)$  and  $\chi_{ch}(q)$ . They are obtained by evaluating  $\chi_{sp}(q)$  and  $\chi_{ch}(q)$  direct space representation at the same point and writing the Fourier series for this same point evaluation in terms of  $\chi_{sp}(q)$  and  $\chi_{ch}(q)$ . By doing this one obtains:

$$\frac{T}{N} \sum_{\mathbf{q}} \sum_{iq_n} \frac{\chi_0(q)}{1 - \frac{1}{2}U_{sp}\chi_0(q)} = n - 2 \langle n_{\uparrow}n_{\downarrow} \rangle \quad (\text{Sum1})$$

$$\frac{T}{N} \sum_{\mathbf{q}} \sum_{iq_n} \frac{\chi_0(q)}{1 + \frac{1}{2}U_{ch}\chi_0(q)} = n + 2 \langle n_{\uparrow}n_{\downarrow} \rangle - n^2 \quad (\text{Sum2})$$

where the right hand side is obtained by using the Pauli exclusion principle. From here, all the main equations of TPSC are set.

The first step of TPSC consists in calculating the Lindhard function  $\chi_0(q)$  (density-density response function for the free Hubbard model). It is obtained using the non-interacting Matsubara Green's function (see [6] chap. 39 sec.2) that is expressed like

$$\mathcal{G}^0(q) = \frac{1}{iq_n - \epsilon(\mathbf{q}) + \mu}$$

where  $\epsilon$  is the non-interacting energy from sec. IV and  $\mu$  is the non-interacting chemical potential associated with the density given as an input parameter. Knowing  $\chi_0(q)$  leave only one unknown in eq. Sum1. Indeed, injecting the  $U_{sp}$  ansatz in eq. Sum1, leads to

$$\frac{T}{N} \sum_{\mathbf{q}} \sum_{iq_n} \frac{\chi_0(q)}{1 - \frac{1}{2} \frac{\langle n_{\uparrow}n_{\downarrow} \rangle}{\langle n_{\uparrow} \rangle \langle n_{\downarrow} \rangle} \chi_0(q)} = n - 2 \langle n_{\uparrow}n_{\downarrow} \rangle.$$

This is an equation of one unknown ( $\langle n_{\uparrow} \rangle \langle n_{\downarrow} \rangle$ ) which is can be determined by solving for it numerically.

Now that the double occupation is to know, it can be injected with  $\chi_0(q)$  in eq. Sum2. Despite having a clear ansatz for  $U_{ch}$ , it is still possible to solve for it because it has become the only unknown of eq. Sum2.

Frequency Type	Part	Symbol
Matsubara	Imaginary	$\text{Im } \Sigma$
Matsubara	Real	$\text{Re } \Sigma$
Real	Imaginary	$\Sigma'$
Real	Real	$\Sigma''$

TABLE I. Notation for the real and imaginary parts of self-energy in Matsubara frequencies and real frequencies

Finally,  $U_{sp}$  and  $U_{ch}$  are determined in a way that forces them to respect the Pauli exclusion principle. With their associated response functions, it is possible to compute a second order self-energy that has the following expression

$$\Sigma_{\sigma}^{(2)}(k) = U_{n-\sigma} + \frac{U}{8} \frac{T}{N} \sum_q [3U_{sp}\chi_{sp}(q) + U_{ch}\chi_{ch}(q)] G_{\sigma}^{(1)}(k+q).$$

Disorder can be added to TPSC calculations by adding a disorder self-energy  $\Sigma^{imp}$  to the non-interaction Green's function. In the clean limit, this self-energy is computed by averaging over the impurities of the system which leads to  $\Sigma^{imp} = -i/(2\tau)$  where  $\tau$  is the scattering time associated to impurities. The resulting greens function is

$$\mathcal{G}^0(q) = \frac{1}{iq_n - \epsilon(\mathbf{q}) + \mu + i/(2\tau)}$$

To match with experiments  $\tau$  was set to 46 in all disorder calculations.

## VI. RESULTS

### A. Power law for the electron-electron scattering rate (without disorder)

To obtain the temperature dependence for the electron-electron scattering rate, self-energy can be used. In simple terms, self-energy is the energy a system has due to the interaction of its particles. For a more detailed phenomenological description of the concept see [6] chap. 17. Table I shows the different self-energy notation used through my report. Note that it is different for Matsubara and real frequency self-energies. The self-energy analysis done here is described in more detail in appendix B of [10]. The first step consists in Taylor expanding the imaginary part of self-energy about  $\omega = 0$  on the Matsubara frequency axis. It leads to

$$\text{Im}\Sigma(\mathbf{k}, i\omega_n) = \text{Im}\Sigma(\mathbf{k}, 0) + \left. \frac{\partial \text{Im}\Sigma(\mathbf{k}, i\omega)}{\partial \omega} \right|_{\omega=0} \omega_n + \dots$$

With the following expression for the quasiparticle weight  $Z_{\mathbf{k}}$

$$Z_{\mathbf{k}} = \frac{1}{1 - \left. \frac{\partial \text{Im}\Sigma(\mathbf{k}, i\omega)}{\partial \omega} \right|_{\omega=0}}$$

the Taylor expansion can be written like

$$\text{Im}\Sigma(\mathbf{k}, i\omega_n) = \text{Im}\Sigma(\mathbf{k}, 0) + \left(1 - \frac{1}{Z_{\mathbf{k}}}\right) \omega_n + \dots$$

This suggests that the linear behaviour of self-energy at sufficiently low frequencies on the Matsubara frequency axis can be used to extract both  $Z_{\mathbf{k}}$  and  $\text{Im}\Sigma(\mathbf{k}, 0)$ . These two quantities are enough to compute the electron-electron scattering rate ( $\gamma_{\mathbf{k}} = -Z_{\mathbf{k}}\text{Im}\Sigma(\mathbf{k}, 0)$ ). Since most of the temperature dependence comes from  $\text{Im}\Sigma(\mathbf{k}, 0)$ , this section will focus on it. Nevertheless, the calculation of  $\gamma_{\mathbf{k}}$  is done in sections VIF.

Matsubara frequencies being discrete, knowing their associated self-energies leads to an approximative Taylor series. Considering only the two smallest frequencies ( $\omega_0$  and  $\omega_1$ ), the Taylor series can be truncated to leave only its linear part. This part is dominant at low frequencies. In the end, one can approximate  $\text{Im}\Sigma(\mathbf{k}, 0)$  and  $Z_{\mathbf{k}}$  by passing a line through points associated to  $\omega_0$  and  $\omega_1$  (see fig. 9). The corresponding approximative expressions are

$$1 - \frac{1}{Z_{\mathbf{k}}} \approx \frac{\text{Im}\Sigma(i\omega_1) - \text{Im}\Sigma(i\omega_0)}{\omega_1 - \omega_0},$$

$$\text{Im}\Sigma(0) \approx \frac{\omega_1 \text{Im}\Sigma(i\omega_0) - \omega_0 \text{Im}\Sigma(i\omega_1)}{\omega_1 - \omega_0}.$$

To obtain the temperature dependence of  $\text{Im}\Sigma(\mathbf{k}, 0)$  which is very similar to that of  $\gamma_{\mathbf{k}}$ , TPSC calculations (see sec. V) were performed for different temperatures and dopings. For each of those calculations, the self-energies were saved for different angles  $\theta$  on the Fermi surface. Finally, self-energy data was fitted to extract  $\text{Im}\Sigma(\mathbf{k}, 0)$ . Making all the dependencies explicit, one writes  $\text{Im}\Sigma(\mathbf{k}(\theta), T, x, 0)$ .

To directly extract an approximative power law for the electron-electron scattering rate temperature dependence,  $\text{Im}\Sigma(\mathbf{k}(\theta), T, x, 0)$  is fitted with the model  $aT^{\nu}$ . The fit parameter  $\nu$  gives the power law and it depends on  $x$  and  $\theta$ . This exponent is plotted against angles on the Fermi surface for different densities (one for each plot) on fig. 10.

The plots for density going from 1.18 to 1.187 show missing points when they are compared to others. These missing points correspond to temperature dependencies that could not be fitted with the  $aT^{\nu}$  model. This is due to the fact that the pseudogap opens at a small enough temperature for these dopings.  $\text{Im}\Sigma(\mathbf{k}(\theta), T, x, 0)$  for low enough temperatures are affected by the pseudogap, making them lose their power law behaviour at high enough angles (close to angles at which the pseudogap opens). Looking at fig. 7, it is possible to locate these plots more precisely. They are produced using TPSC results for fixed doping and varying temperature, therefore they can be associated to vertical lines on fig. 7. If the vertical line crosses  $T^*$  at some point, the power



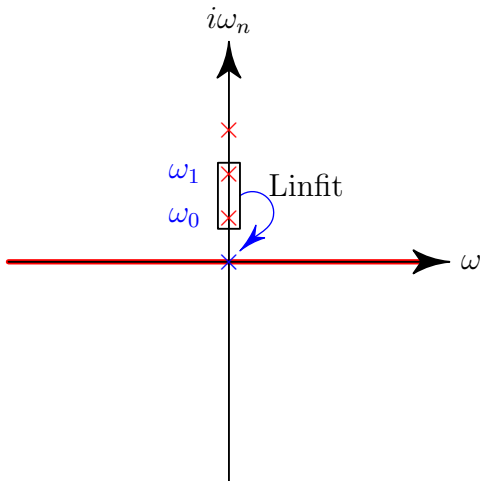


FIG. 9. Schematic representation of the linear extrapolation from the first two Matsubara frequencies to the zero frequency evaluation of self-energy

la behaviour of the temperature dependence is partially lost. The extent to which it is lost is related to the range of temperatures for which TPSC calculations were performed below the  $T^*$  line. As the doping gets closer to the QCP doping  $x_c$  the range of TPSC calculations affected by the pseudogap gets smaller and the fits start working better for every angle. Even tho they stop completely failing, the exponents only begin to be meaningful when it approaches 1 (linearity) at  $45^\circ$ . For  $n = 1.20$  the behaviour is close to being linear at the nodal point and this is an important characteristic of a non-Fermi liquid behaviour typically observed in the quantum critical region. Since this linear behaviour is not perfect (the exponent is bigger than 1)  $n = 1.20$  is associated to a doping beyond the QCP doping. For high enough dopings and low enough temperature, the power law is expected to become quadratic which is a Fermi liquid characteristic (see the separation of the Fermi and non-Fermi liquid behaviour in fig. 7). The extent to which it is quadratic is related to the proportion of TPSC calculations done in the Fermi liquid region in comparison with the number of calculations done in the non-Fermi liquid region. For the highest dopings in 10, a quadratic temperature dependence of the electron-electron scattering rate is observed. This means that the TPSC calculations for these dopings are mostly associated to points below the Fermi liquid separation line.

It would be interesting to perform more precise calculation between  $n = 1.19$  and  $n = 1.20$  to locate the QCP by looking for a perfect linear behaviour at high angles.

## B. Fits on real frequency self-energy

It is possible to verify the Fermi liquid behaviour for small angles at  $x \approx 19\%$  suggested by the Matsubara frequency analysis of sec. VIA with a real frequency analysis. This Fermi liquid behaviour is displayed in the first column/second row plot in fig. 10 where there is a clear quadratic dependency on temperature for small angles. The results of this section aim to make the temperature dependency of self-energy at low frequencies more precise. They are obtained by using TPSC calculations for many temperatures and many interaction strengths  $U$  (see sec.IV). For each of those calculations, self-energy data is saved at the antinodal point where the Fermi-liquid behaviour is expected to be maximal. Self-energy curves from these calculations are plotted for different  $U$  values and an example temperature in fig. 11

From Matsubara self-energy curves, it is possible to obtain self-energy evaluated at real frequencies by analytically continuing Matsubara frequency results to real frequency ones. The method used here is based on padé approximants (see [11] chap. 9). By example, applying it to the curves of fig. 11 the curves in fig. 12.

In [12] a low frequency expression for the imaginary part of the self-energy of a Fermi liquid is given. Using the Kamers-Kronig relation the real part is then obtained. The real and imaginary parts of self-energy have the following forms

$$\Sigma'(\omega) \approx b_0 + a_1\omega, \quad (\text{Fit1})$$

$$\Sigma''(\omega) \approx a_0 - a_2\omega^2. \quad (\text{Fit2})$$

Using these expressions as fit models for low frequency self-energy, we can extract values for the fit parameters  $b_0$ ,  $a_0$ ,  $a_1$  and  $a_2$  from each of the self-energy curves for  $U$  values and  $T$ . In the end, the fit parameters can be seen as functions of temperature and interaction  $U$ . Table II show the expected dependencies on temperature of each parameter for a Fermi liquid : the only parameter that is expected to depend on temperature is  $a_0$  and it depends on  $T^2$ . Note that the  $U^2$  dependencies for every parameter are not a result of Fermi liquid theory: they are results from second-order perturbation theory.

When the fit parameters are plotted against  $T^2$  while keeping curves for different  $U$  values differentiated by colour, fig. 13 is produced. While  $b_0$  and  $a_1$  show approximately no dependence on temperature,  $a_2$  shows a little dependence which is overly amplified by the misleading fit on the brown data. The clear dependence on temperature is seen in the  $a_0$  plot. This dependence is quadratic and the Fermi liquid behaviour is confirmed both by the Matsubara and real frequency analysis. Finally, fig. 15 shows that the result of second-order perturbation theory is also verified.



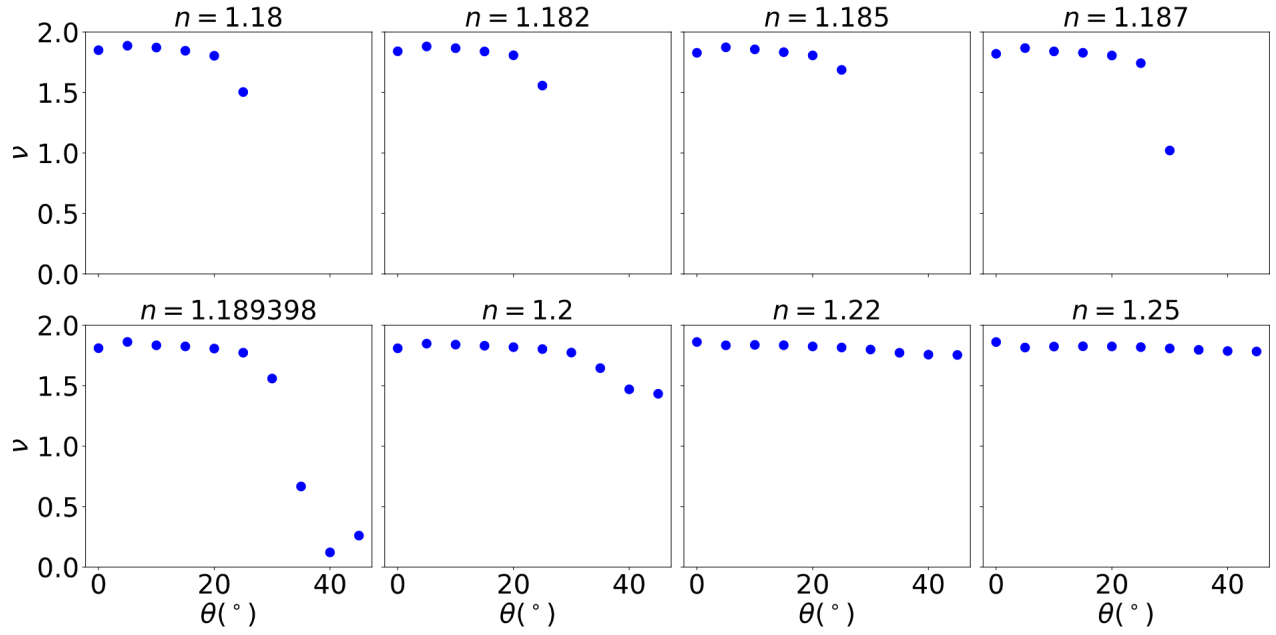


FIG. 10. Exponent  $\nu$  giving the power law for the temperature dependance of the imaginary part of self-energy at zero frequency as a function of angle on the Fermi surface for different dopings (without disorder at  $U = 5.75$ )

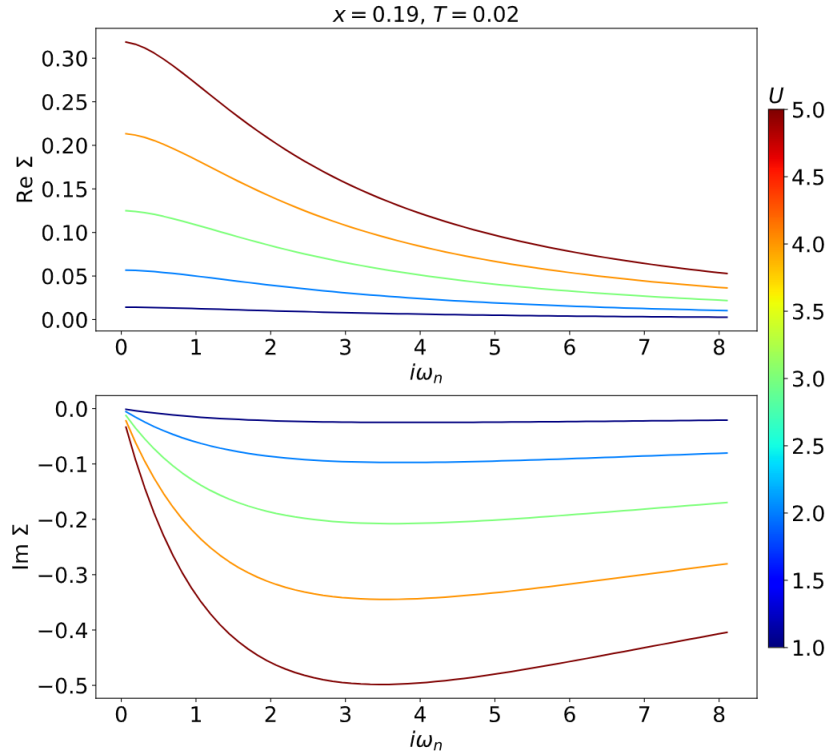


FIG. 11. Self-energy curves for matsubara frequencies for a fixed temperature and varying interaction  $U$

### C. Kadowaki-Woods ratio

It was shown in sec. VIB that there is a clean Fermi liquid behaviour for simulated NCCO at the antinodal

point for a doping of 19%. An interesting result obtained experimentally for Fermi liquids is the Kadowaki-woods relation. It makes a link between the quasiparticle weight ( $Z$ ) and the temperature independent coefficient of the quasiparticle lifetime (related to  $a_2$  from eq. Fit2).

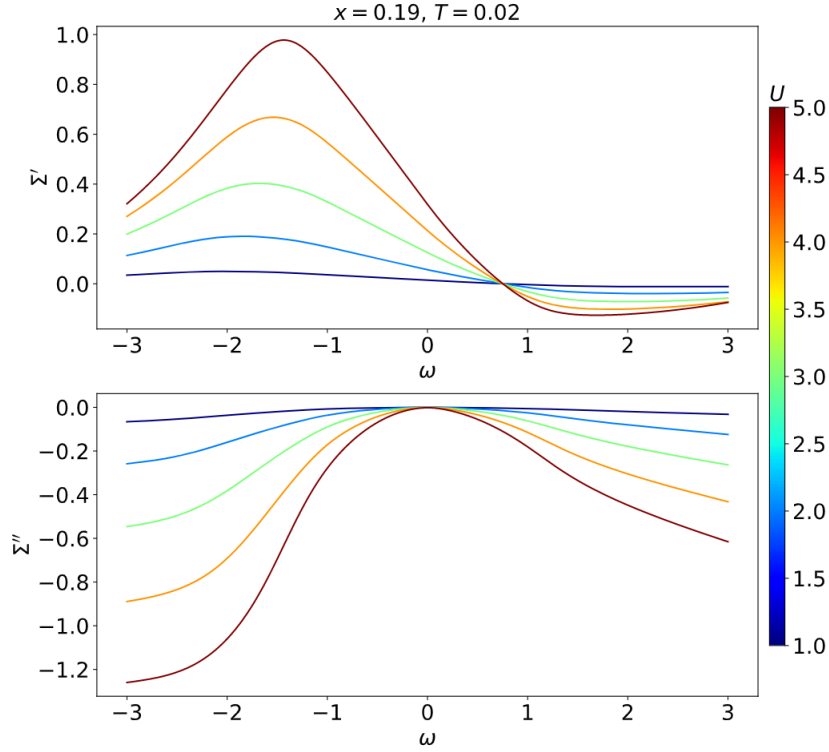


FIG. 12. Self-energy curves for real frequencies for a fixed temperature and varying interaction  $U$

Parameter	Proportionnal to	Associated to
$a_0$	$T^2, U^2$	Scattering rate
$a_1$	$U^2$	Quasiparticle weight
$a_2$	$U^2$	Scattering rate
$b_0$	$U^2$	

TABLE II. Associations and expected dependencies on Temperature (from Fermi liquid theory) and interaction  $U$  (from second order perturbation theory) for the fit parameters  $a_0$ ,  $a_1$ ,  $a_2$ ,  $b_0$

With data described in sec. VIB it is possible to produce a Kadowaki-woods plot that is an analogue of the one obtained with ARPES measurements in [3]. Here we can access the quasiparticle weight and the quasiparticle lifetime with the data for different temperatures and  $U$  values.

Since the quasiparticle weight is defined to be

$$Z = \frac{1}{1 - \left. \frac{\partial \Sigma'(\mathbf{k}, \omega)}{\partial \omega} \right|_{\omega=0}},$$

it can be extracted from the  $a_1$  fit parameter in eq. (Fit1) which corresponds to the first derivative of the real part of self-energy at low frequencies (where eq. (Fit1) applies). Knowing this, one can write  $Z = 1/(1 - a_1)$  and use the  $a_1$  plot from fig. 15 to produce a plot of  $Z$  against  $U^2$  (see fig. 17). This plot

shows the dependency on interaction of the quasiparticle weight: when  $U$  is small the physics of NCCO is well described by the concept of quasiparticles ( $Z \approx 1$ ), but when  $U$  increases,  $Z$  decreases as the concept of quasiparticle gets less relevant in the description of the system.

Plotting  $a_2$  (from fig. 18) against  $1/Z^2$ , yields the Kadowaki-woods relation displayed in fig. 19. This result suggests that there is a slight temperature dependency for the Kadowaki-woods ratio. This temperature dependence arises from  $a_2$  (it may be caused by residual non-Fermi liquid behaviour) and it can be seen in fig. 15. While, the data for this plot was obtained using TPSC calculations for different  $U$  values and different temperatures, the experimental result in [3] was produced using ARPES data for different materials. Nevertheless, a linear relation is observed between  $1/Z^2$  and  $a_2$  suggesting that a universal ratio (the Kadowaki-woods) is present across a wide range of materials and interactions  $U$  for NCCO.

#### D. Locating the Quantum critical point with disorder

To simulate NCCO in a more realistic way, disorder can be added to TPSC calculations (see sec. V). Studying the effects of disorder on theoretical accuracy starts with a localization of the QCP in the presence of disorder.

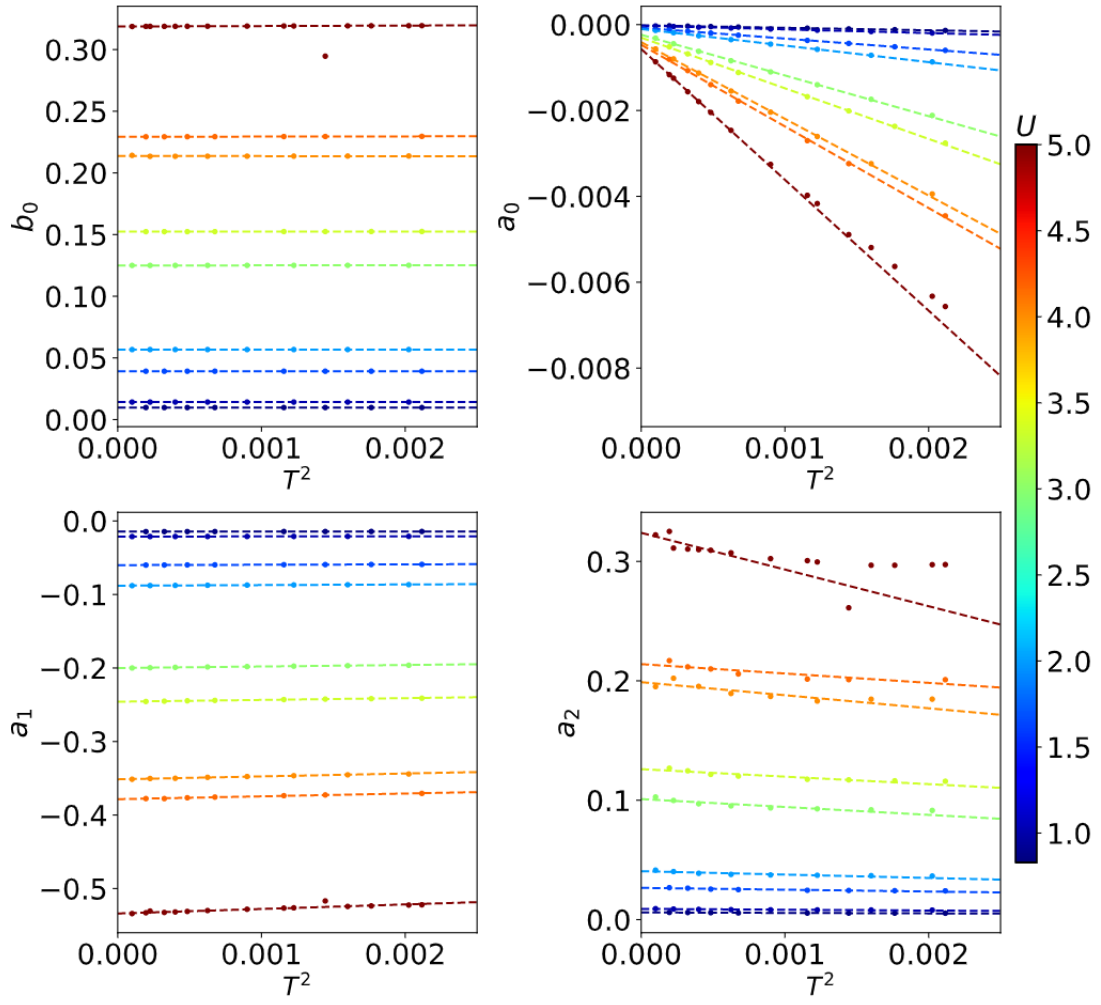


FIG. 13. Fit parameters as functions of  $T^2$  for different interaction  $U$  values associated to colours

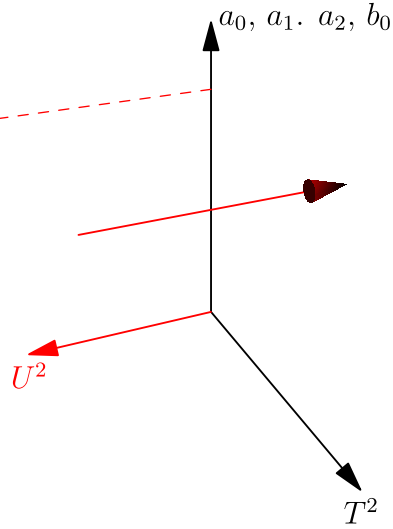


FIG. 14. Schematic representation of the projection of the  $U^2$  axis to the  $T^2$ -parameter plane

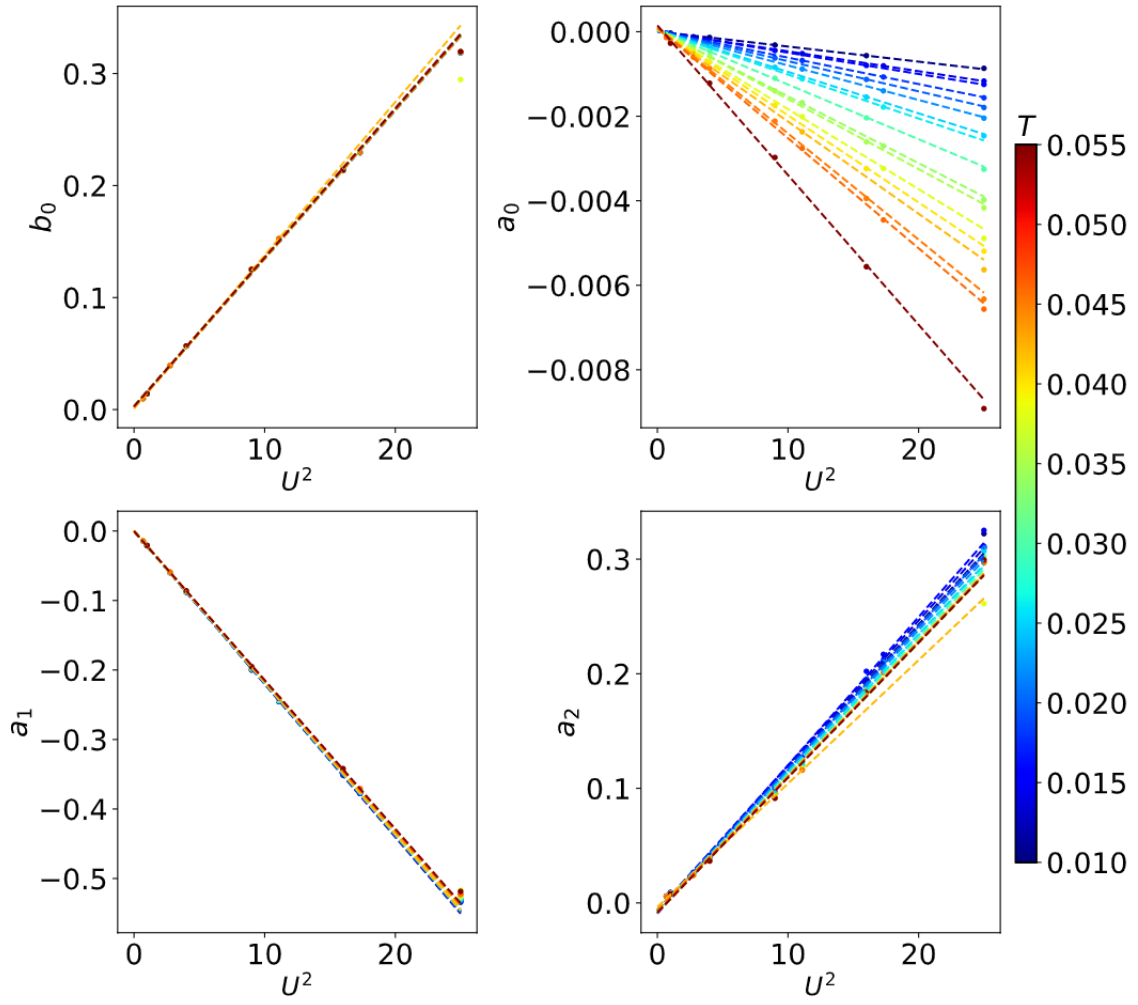


FIG. 15. Fit parameters as functions of  $U^2$  for different temperatures values associated to colours

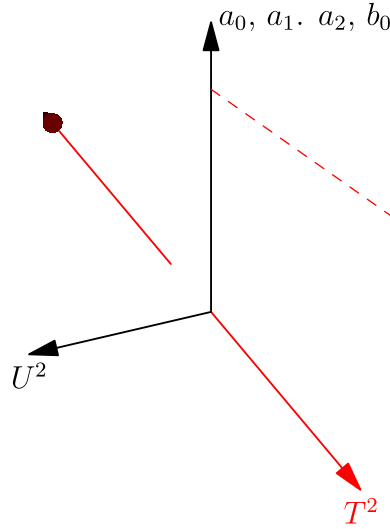


FIG. 16. Schematic representation of the projection of the  $T^2$  axis to the  $U^2$ -parameter plane

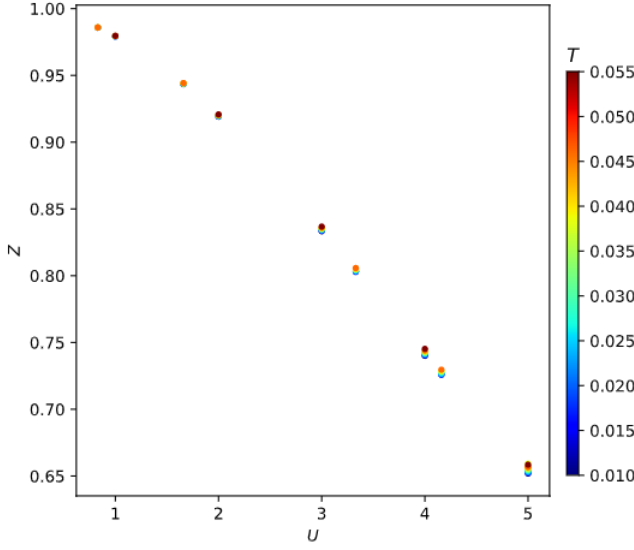


FIG. 17. Quasiparticle weight  $Z$  as a function of the interaction  $U$  for different temperatures giving the colour

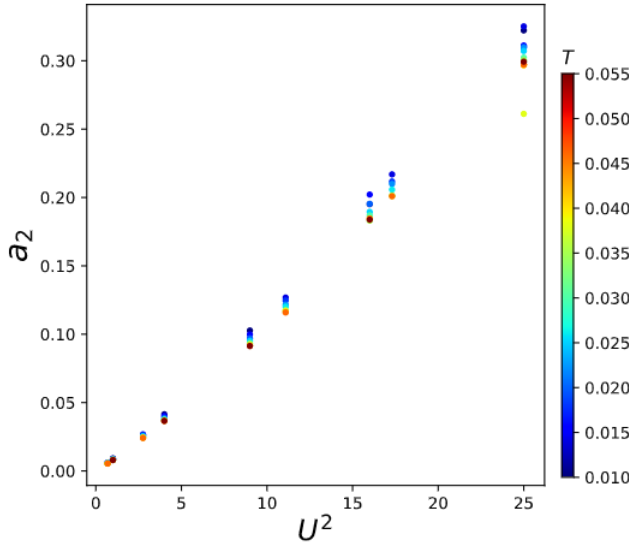


FIG. 18.  $a_2$  fit parameter as a function of  $U^2$  for different temperatures

der. As far as the two-dimensional model without disorder goes, the QCP is located at the doping where the pseudogap opens at zero temperature. In the end, calculations suggested that this fact doesn't change when disorder is added. Because of the limitations of TPSC at small dopings, the data was not enough to conclude on that matter but it suggested that the QCP was not far enough from the pseudogap point to make it clear they were separated. This is important because the present analysis is based on extrapolation from points on the  $T^*$  line to a point at zero temperature which is taken to be the QCP. Further calculations (see sec. VIF) assuming

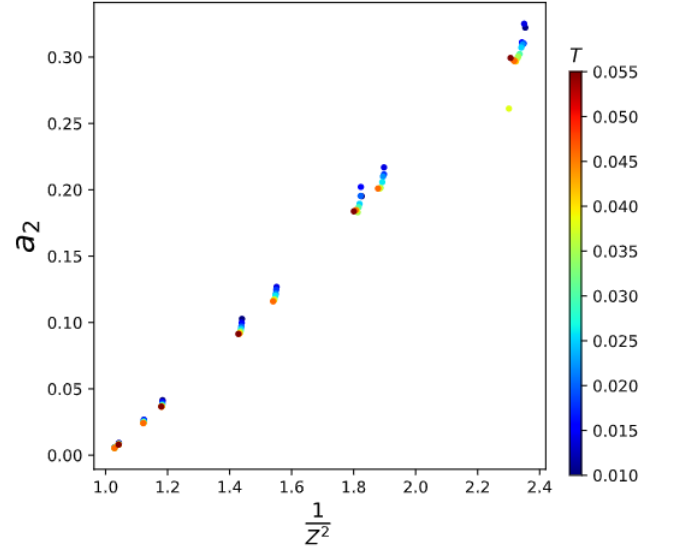


FIG. 19. Kadowaki-woods plot

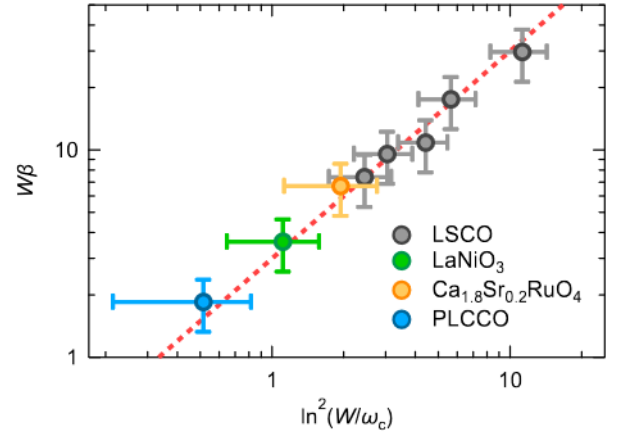


FIG. 20. Spectroscopic Kadowaki-woods plot [3]

this point was the AFM QCP have led to the right quantum critical behaviour above this so-called QCP. This is a good sign that the  $T^*$  point is very close or coincident with the AFM QCP.

Knowing that  $T^*$  leads to the QCP, locating the QCP reduces to finding points on  $T^*$  and performing a linear extrapolation to the  $T = 0$  axis. Two approaches were used here to achieve this. The first one consists in using animations of  $A(\mathbf{k}, \omega = 0)$  as it evolves with doping for a given temperature (every frame is a spectral weight calculated or the result of a linear interpolation of intensities between calculated  $A(\mathbf{k}, \omega = 0)$  frames). For this particular temperature  $T^*$ , the highest doping at which a loss in spectral weight can be visually noticed is noted  $x^*$ . Combined with its associated temperature, this doping forms a point on the  $T^*$  line. Repeating the process of visually finding  $x^*$  for three different temperatures yields points displayed in fig. 21 (using

animations without disorder added) and fig. 22 (using animations with disorder added). The blue lines represent fits on the three points : these fits are extended to the point they cross the doping axis. The exact values of both linear extrapolations are not very relevant here. Since this approach is rather subjective, its results are not taken too seriously. Nevertheless, they imply that adding disorder shifts the QCP to lower doping. The red and green lines are a guide to see how the uncertainty of the points (determined visually) leads to uncertainty of the extrapolated QCP.

The second approach is more precise and relies on the manifestation of the opening of the pseudogap in the spectral weight as a function of  $\omega$  at hot-spots. Here, Hot-spots are points close to where the pseudogap opens in the Brillouin zone. They are defined as the intersection point between the non-interacting Fermi surface and the AFM Brillouin zone boundary (see fig. 23 and sec. II where the AFM Brillouin zone is discussed). The non-interacting Fermi surface is itself defined as the set of points satisfying  $\epsilon(\mathbf{k}) = \mu$  where  $\mu$  is the non-interacting chemical potential associated with the doping and  $\epsilon(\mathbf{k})$  is the dispersion relation from the non-interacting Hubbard model given in sec. IV. Knowing the location of the hot-spots, the TPSC calculations lead to self-energy curves as functions of Matsubara frequencies at those points. Performing analytic continuation with padé approximants on those curve, one gets real frequency self-energy curves. This data is directly related to the spectral weight as a function of  $\omega$  at hot-spots with the following expression

$$A(\mathbf{k}_F, \omega) = -\frac{1}{\pi} \text{Im} \left[ \frac{1}{\omega - \epsilon(\mathbf{k}_F) + \mu^{(2)} - \Sigma^{(2)} - \Sigma^{Imp}} \right]$$

where  $\mathbf{k}_F$  refers to the hot-spot coordinates,  $\mu^{(2)}$  is the second order interacting chemical potential associated to the doping,  $\Sigma^{(2)} = \Sigma' + i\Sigma''$  is the self-energy from padé approximants and  $\Sigma^{Imp}$  is the disorder self-energy mentioned in sec. V.

In the end the spectral weight at hot-spots as a function of  $\omega$  can be obtained using TPSC calculations for a set of temperature and dopings. The result is displayed on fig. 25. In this figure, one can observe that there are two types of spectral weight curves which are represented schematically in fig. 24. The red curve represents spectral weight at hot-spots for dopings and temperatures above the  $T^*$  curve : it shows the typical look of the spectral weight curve when the pseudogap hasn't opened. On the other side, the green and blue curves have a local minima at  $\omega = 0$  and are associated to dopings and temperatures for which the pseudogap has opened. For each plot in fig. 25, the temperature is fixed and the doping varies to produce many different spectral weight curves (distinguished with coloration). This allows to see the pseudogap appearance more precisely. The doping  $x^*$  at which the pseudogap opens for each temperature was taken to be the second-highest

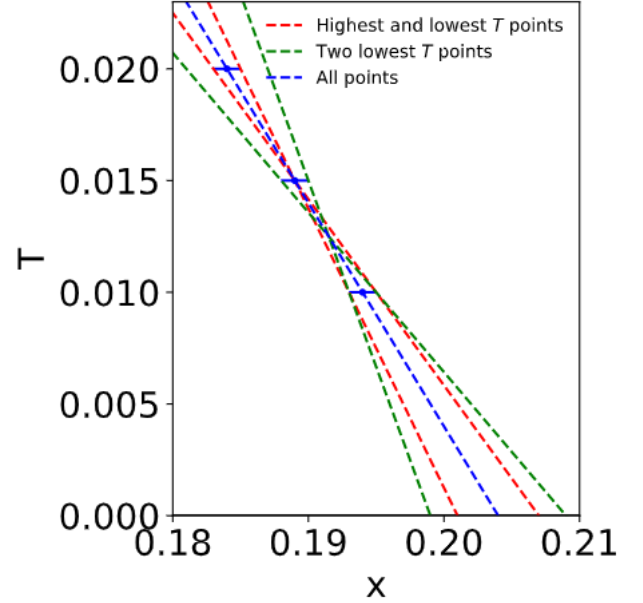


FIG. 21. Linear extrapolation estimating the doping of the quantum critical point using the doping at which the pseudogap opens for different temperatures (without disorder)

doping for which there is a local minimum in spectral weight at the hot-spots. Suppose the green curve from fig. 24 is associated to the highest doping for which a local minimum is found and the blue curves is the next highest doping with a local minimum. To remove some aberrant points, the equivalent of the green curve was skipped and the equivalent of the blue curve's doping was taken to be  $x^*$ .

All this analysis led to the  $T^*$  plot of fig. 26. Keep in mind that the extrapolated position for the QCP doping might undervalued because of the process by which  $x^*$  was selected. While the five points with lowest dopings seem to be on the same line, the three highest doping points show a different behaviour and they were considered to be aberrant data (probably associated to convergence failure in TPSC calculations at low temperature but the cause is not very clear). The QCP doping suggested by all the points is  $x_c \approx 0.189$  and the one suggested by the three aberrant points only is  $x_c \approx 0.183$ . Calculations at the QCP doping were done at  $x_c \approx 0.189$ .

#### E. Criteria for the pseudogap opening with disorder

With the coordinates for points close to  $T^*$ , it is possible to check if disorder solves an important theoretical inconsistency. This inconsistency arises when the spin correlation length  $\xi_{sp}$  and thermal de Broglie length  $\xi_{th}$  are computed and compared at different points of  $T^*$ . Here, the spin correlation length is defined to be the



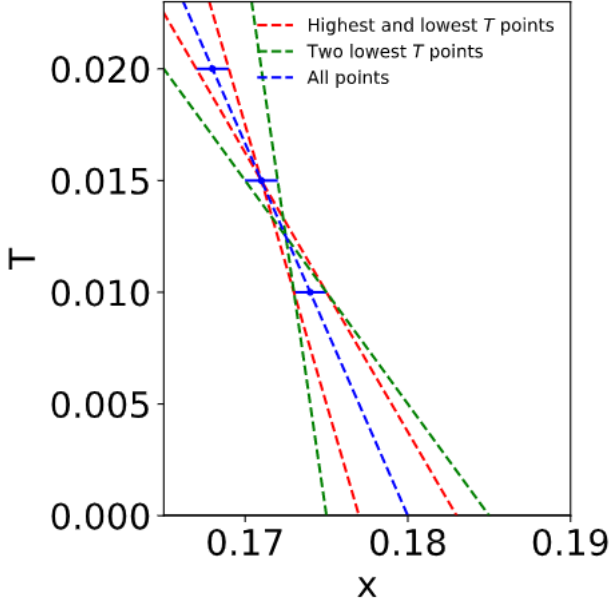


FIG. 22. Linear extrapolation estimating the doping of the quantum critical point using the doping at which the pseudo-gap opens for different temperatures (with disorder)

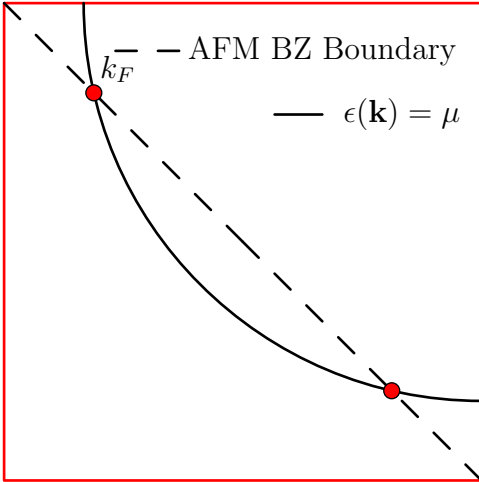


FIG. 23. Schematic representation of the definition of hot-spots in a quarter Brillouin zone

FWHM of the local spin response function. The thermal de Broglie length is defined as  $\xi_{th} = v_F/(\pi T)$  with the Fermi velocity  $v_F$ . While TPSC calculations without disorder produce values of  $\xi_{sp}$  and  $\xi_{th}$  that respect  $\xi_{sp} > \xi_{th}$ , experimental data only agrees with this order for points on  $T^*$  below a doping of 15%. For higher dopings on  $T^*$ , experimental data suggest  $\xi_{sp} < \xi_{th}$  instead.

One of the goals of the implementation of disorder to TPSC calculations was to reproduce this inversion of the order relation beyond a certain doping. For each  $T^*$  point

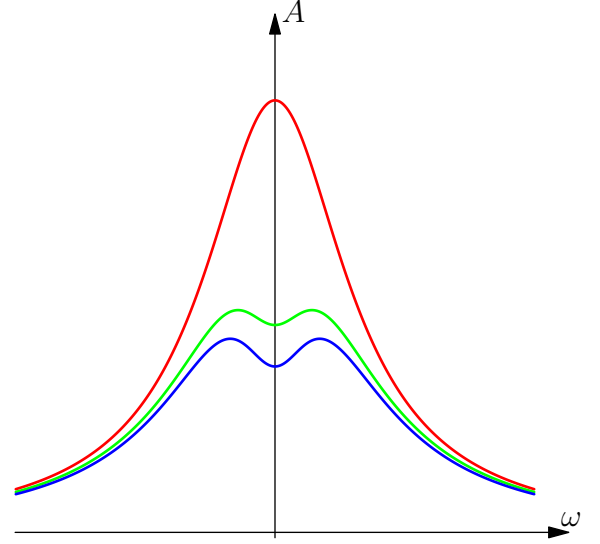


FIG. 24. Schematic representation of the different types of Spectral weight curves at the hot spots

of fig. 26,  $\xi_{sp}$  and  $\xi_{th}$  were computed. To highlight the possible effect of disorder on these lengths the mean free path associated to impurity  $L = v_F\tau$  was also computed for all  $T^*$  points. Plotting all these lengths against the  $x^*$  doping associated to the  $T^*$  point they were computed at, one gets fig. 27. This figure leads to the conclusion that the order relation  $\xi_{sp} > \xi_{th}$  is valid everywhere on  $T^*$  even if disorder is added. Therefore, the experimental observation cannot be explained by disorder in the clean limit. This is consistent with the fact that the mean free path is always larger than  $\xi_{sp}$  and  $\xi_{th}$ . Finally, note that the last three points (highest  $x^*$ ), again show different behaviour and were not taken too seriously although they seem to lead to an inversion of the order relation.

#### F. Power law for the electron-electron scattering rate (with disorder)

This section repeats the analysis of sec. VIA and focuses on the temperature dependence of the electron-electron scattering rate at the QCP doping  $x_c \approx 0.189$  (see sec. VID). Again, TPSC calculations were performed at different temperatures at fixed doping  $x_c$ . Saving Matsubara frequency self-energy across the Fermi surface, it is possible to find  $\text{Im}\Sigma(0)$  and  $Z$  with a linear extrapolation. Plotting these quantities against temperature for different angles giving the colour yields fig. 28. On this figure the evolution from a Fermi liquid behaviour to non-Fermi liquid behaviour is clear. Both plots show quadratic dependencies on temperature at the antinodal point. Then, moving from the antinode to the node leads the temperature dependence of both  $\text{Im}\Sigma(0)$  and  $-Z\text{Im}\Sigma(0)$  to become linear. This can be made more precise by fitting the curves from fig. 28

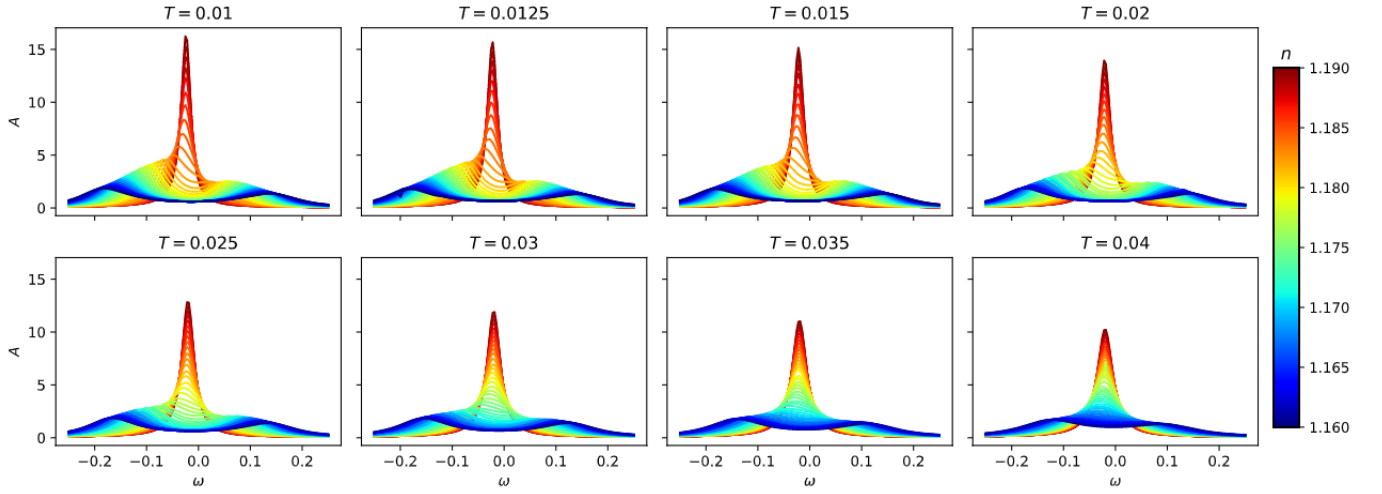


FIG. 25. Spectral weight evaluated at hot spots as a function of frequency for different temperatures (one for each plot) and different dopings (giving the color)

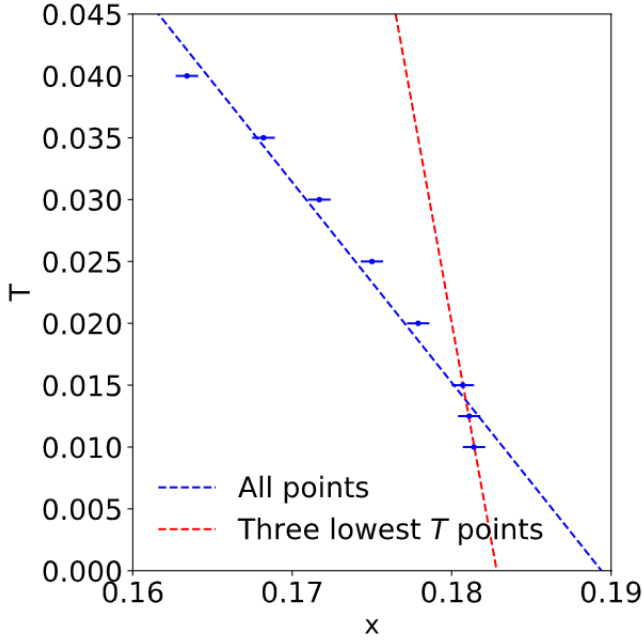


FIG. 26. Linear extrapolation estimating the doping of the quantum critical point using the second biggest doping for which there is a local minima near  $\omega = 0$  in the spectral weight evaluated at the hot-spots as a function of temperature (with disorder)

with the power law model  $aT^\nu$  and plotting the resulting exponent  $\nu$  as a function of the angle labelling the fitted curve (with its associated colour). This leads to fig. 29 where two plateaux can be observed. There is one for angles close to the antinode and a smaller one for angles close to the node. The antinode plateau corresponds to quadratic temperature dependence since  $\nu \approx 2$  and the node plateau is associated to linear dependence on

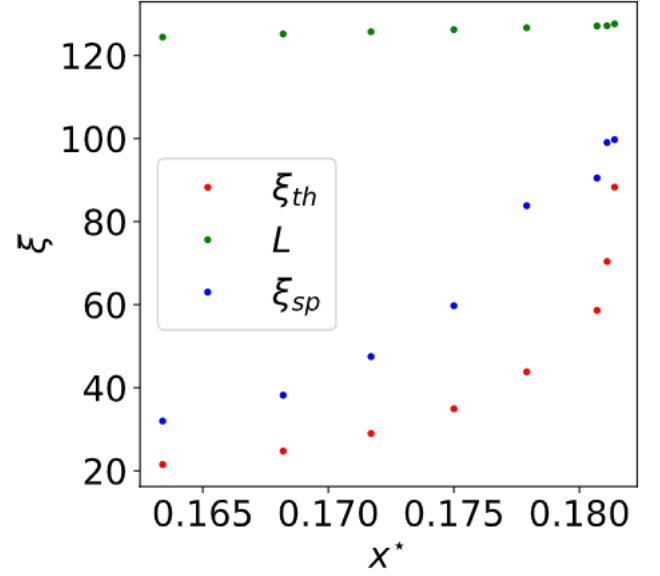


FIG. 27. Order relation between the spin correlation length  $\xi_{sp}$ , the thermal de Broglie length  $\xi_{th}$  and the mean free path  $L$  associated to disorder

temperature  $\nu \approx 1$ . Note that the quadratic behaviour is more intense when  $Z$  is included in the calculations.

Varying doping and doing the power law analysis once again yields the eight plots of fig. 30. The dopings were chosen to match the ones of fig. 10 in order to make comparisons easier. The most interesting fact that comes out of the comparison is the shift of similar plots to lower dopings consistent with the shift of  $x_c$  when disorder is added. Respectively comparing the  $n = 1.182$  and  $n = 1.18$  plots from 30 to the  $n = 1.187$  and  $n = 1.189398$  plots from 30 reveals a shift of about  $-0.007$  of the den-

sities labelling the plots when disorder is added. This suggests that the QCP without disorder is located at around  $n = 1.196$  and it would be interesting to verify if this density indeed has quantum critical properties.

### G. Conclusion

Globally, my analysis focussed on the electron-electron scattering dependence on temperature across the Fermi surface with and without disorder to observe the signature of the QCP. In sec. VIA and VIF, the temperature dependence of the scattering rate across the Fermi surface was studied for many dopings. The comparison of the results of both sections suggests that disorder in the clean limit simply shifts the quantum critical point to a lower doping by an approximative amount of 0.007. From the power law analysis of sec. VIA, the Fermi liquid proper-

ties of NCCO at the antinode for a doping of 19% were studied in sec. VIB with a real frequency analysis. Then, the equivalent of the spectroscopic Kadowaki-woods plot was produced in sec. VIC by varying temperature and interaction strength. In the following section (sec. VID) the location of the QCP with disorder was found using two techniques and was finally taken to be around  $x_c \approx 0.189$ . Knowing this new location allowed to find temperature-linear scattering rate at the node for this critical doping in sec. VIF. In sec. III, it was shown that the addition simple disorder like the one implemented here is not sufficient to explain theoretical inconsistencies. Either a more precise disorder implementation or investigation about other phenomena such as superconductivity seems to be required to produce a clear explanation. The main inconsistency that was treated here is about the relation between the spin correlation length and the thermal De Broglie length for temperatures and dopings on the  $T^*$  line.

- 
- [1] A. Guarino, C. Autieri, P. Marra, A. Leo, G. Grimaldi, A. Avella, and A. Nigro, enSuperconductivity induced by structural reorganization in electron-doped cuprate NCCO, arXiv:2012.13399 [cond-mat] (2020), arXiv: 2012.13399.
  - [2] E. M. Motoyama, G. Yu, I. M. Vishik, O. P. Vajk, P. K. Mang, and M. Greven, enSpin correlations in the electron-doped high-transition-temperature superconductor  $\text{Nd}_{2-x}\text{Ce}_x\text{CuO}_{4 \pm \delta}$ , Nature **445**, 186 (2007), arXiv: cond-mat/0609386.
  - [3] M. Horio, K. P. Kramer, Q. Wang, A. Zaidan, K. von Arx, D. Sutter, C. E. Matt, Y. Sassa, N. C. Plumb, M. Shi, A. Hanff, S. K. Mahatha, H. Bentmann, F. Reinert, S. Rohlf, F. K. Diekmann, J. Buck, M. Kalläne, K. Rossnagel, E. Rienks, V. Granata, R. Fittipaldi, A. Vecchione, T. Ohgi, T. Kawamata, T. Adachi, Y. Koike, A. Fujimori, M. Hoesch, and J. Chang, enOxide Fermi liquid universality revealed by electron spectroscopy, Phys. Rev. B **102**, 245153 (2020), arXiv: 2006.13119.
  - [4] R. L. Greene, P. R. Mandal, N. R. Poniatowski, and T. Sarkar, enThe Strange Metal State of the Electron-Doped Cuprates, Annu. Rev. Condens. Matter Phys. **11**, 213 (2020).
  - [5] A. Reymbaut, Universalité du crossover de Mott à demi-remplissage et effets de la répulsion coulombienne aux premiers voisins sur la dynamique supraconductrice des isolants de Mott dopés aux trous, , 379.
  - [6] A.-M. Tremblay, enPHY-892 Quantum Material's Theory, from perturbation theory to dynamical-mean ... eld theory (lecture notes)., , 759.
  - [7] D. Sénéchal, Introduction à la deuxième quantification et au modèle de hubbard (1999).
  - [8] P. S. H. Simon, Lecture Notes for Solid State Physics (3rd Year Course 6) Hilary Term 2012, , 269.
  - [9] A.-M. S. Tremblay, enTwo-Particle-Self-Consistent Approach for the Hubbard Model, arXiv:1107.1534 [cond-mat] **171**, 409 (2012), arXiv: 1107.1534.
  - [10] T. Schäfer, N. Wentzell, F. Šimkovic IV, Y.-Y. He, C. Hille, M. Klett, C. J. Eckhardt, B. Arzhang, V. Harkov, F.-M. L. Régent, A. Kirsch, Y. Wang, A. J. Kim, E. Kozik, E. A. Stepanov, A. Kauch, S. Andergassen, P. Hansmann, D. Rohe, Y. M. Vilk, J. P. F. LeBlanc, S. Zhang, A.-M. S. Tremblay, M. Ferrero, O. Parcollet, and A. Georges, enTracking the Footprints of Spin Fluctuations: A Multi-Method, Multi-Messenger Study of the Two-Dimensional Hubbard Model, arXiv:2006.10769 [cond-mat, physics:physics] (2021), arXiv: 2006.10769.
  - [11] D. Sénéchal, Méthodes numériques de simulation (2018).
  - [12] A. C. Jacko, J. O. Fjærestad, and B. J. Powell, enA unified explanation of the Kadowaki-Woods ratio in strongly correlated metals, Nature Phys **5**, 422 (2009).

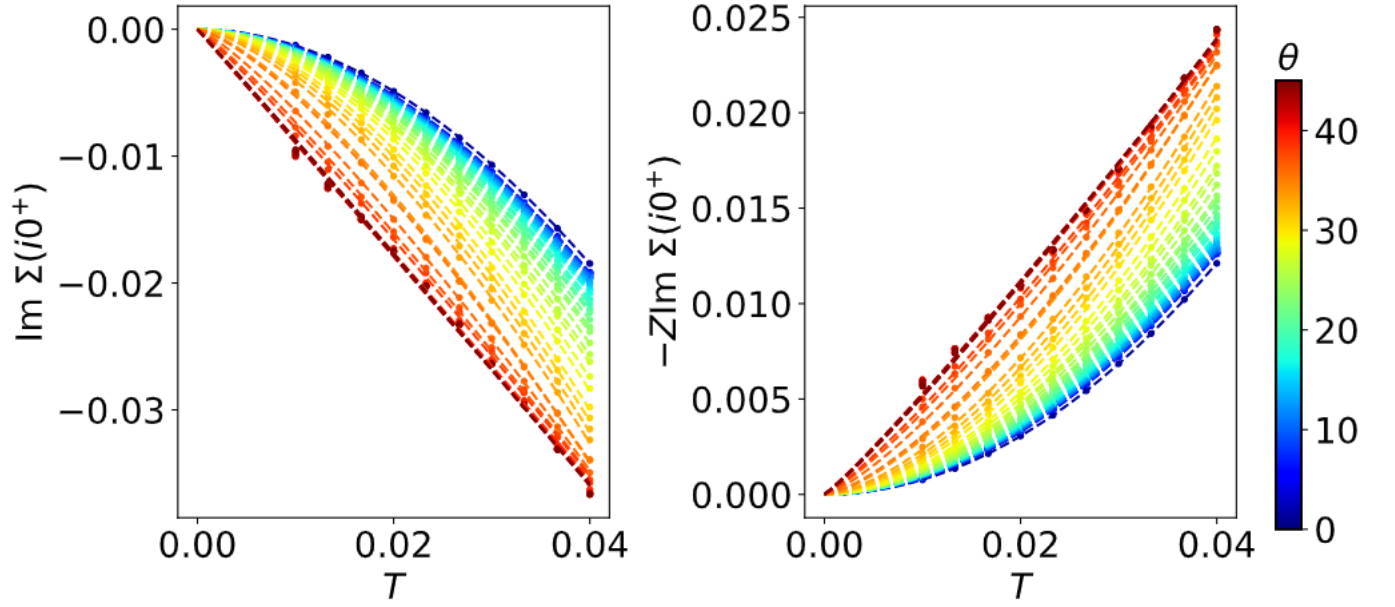


FIG. 28. Imaginary part of self-energy (left) and electron-electron scattering rate (right) as a function of temperatures for different angles on the Fermi surface giving the colour

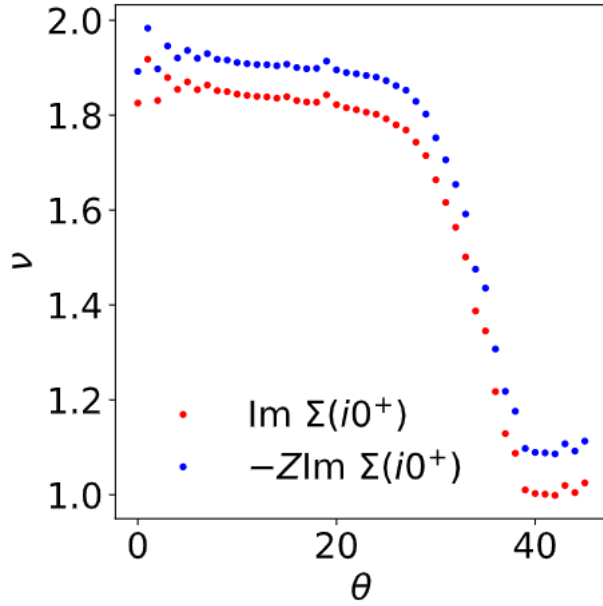


FIG. 29. Exponent  $\nu$  giving the power law for the temperature dependence of the imaginary part of self-energy at zero frequency (blue) and the electron-electron scattering rate (red) as a function of angle on the Fermi surface for the estimated quantum critical doping

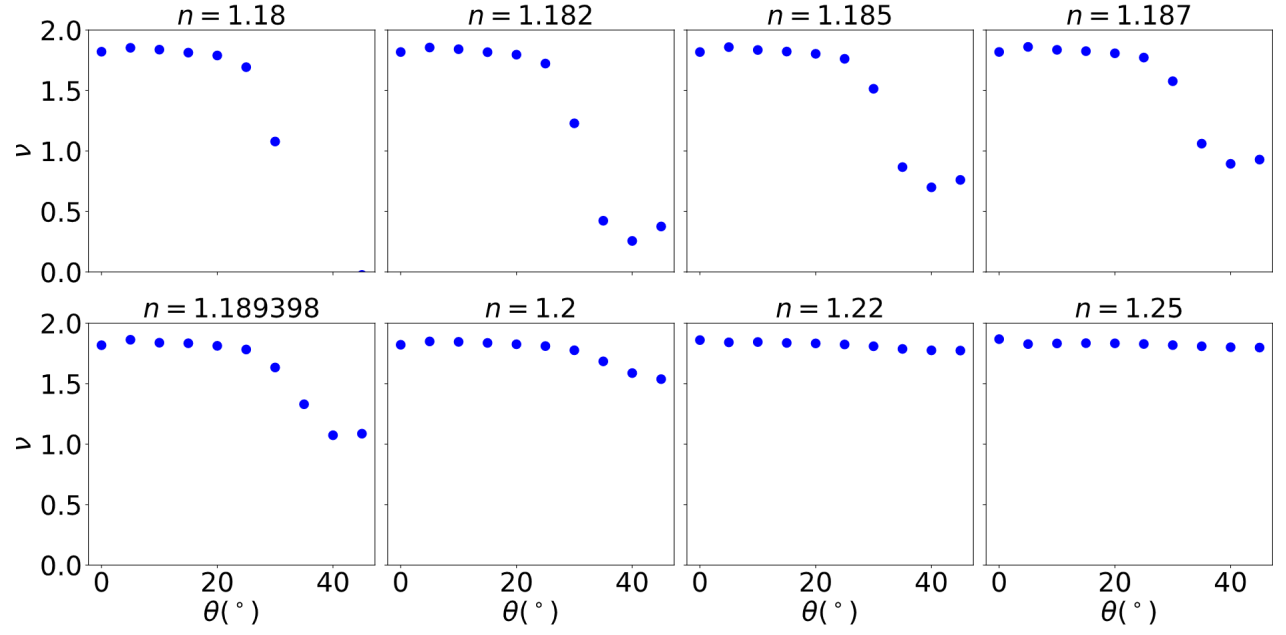


FIG. 30. Exponent  $\nu$  giving the power law for the temperature dependance of the imaginary part of self-energy at zero frequency as a function of angle on the Fermi surface for different dopings (with disorder associated to the impurity scattering time  $\tau = 46$  at  $U = 5.75$ )